Remote Sens. **2015**, *7*, 5160-5186; doi:10.3390/rs70505160

OPEN ACCESS

remote sensing

ISSN 2072-4292

www.mdpi.com/journal/remotesensing

Article

Hyperspectral REE (Rare Earth Element) Mapping of Outcrops—Applications for Neodymium Detection

Nina Kristine Boesche [1,2,*], Christian Rogass [1], Christin Lubitz [1], Maximilian Brell [1], Sabrina Herrmann [1], Christian Mielke [1,2], Sabine Tonn [1], Oona Appelt [1], Uwe Altenberger [2] and Hermann Kaufmann [1]

[1] GeoForschungsZentrum Potsdam, Helmholtz Zentrum, Telegrafenberg, 14473 Potsdam, Germany; E-Mails: rogass@gfz-potsdam.de (C.R.); christin.lubitz@gfz-potsdam.de (C.L.); brell@gfz-potsdam.de (M.B.); saherrma@gfz-potsdam.de (S.H.); chmielke@gfz-potsdam.de (C.M.); sabine.tonn@gfz-potsdam.de (S.T.); oona.appelt@gfz-potsdam.de (O.A.); charly.kaufmann@web.de (H.K.)

[2] Universität Potsdam, Karl-Liebknecht Str. 24-2514476 Potsdam-Golm, Germany; E-Mail: altenber@uni-potsdam.de

* Author to whom correspondence should be addressed; E-Mail: nina.boesche@gfz-potsdam.de; Tel.: +49-331-288-28775; Fax: +49-331-288-1192.

Academic Editors: Richard Gloaguen and Prasad S. Thenkabail

Received: 9 October 2014 / Accepted: 20 April 2015 / Published: 24 April 2015

Abstract: In this study, an *in situ* application for identifying neodymium (Nd) enriched surface materials that uses multitemporal hyperspectral images is presented (HySpex sensor). Because of the narrow shape and shallow absorption depth of the neodymium absorption feature, a method was developed for enhancing and extracting the necessary information for neodymium from image spectra, even under illumination conditions that are not optimal. For this purpose, the two following approaches were developed: (1) reducing noise and analyzing changing illumination conditions by averaging multitemporal image scenes and (2) enhancing the depth of the desired absorption band by deconvolving every image spectrum with a Gaussian curve while the rest of the spectrum remains unchanged (Richardson-Lucy deconvolution). To evaluate these findings, nine field samples from the Fen complex in Norway were analyzed using handheld X-ray fluorescence devices and by conducting detailed laboratory-based geochemical rare earth element determinations. The result is a qualitative outcrop map that highlights zones that are enriched in neodymium. To reduce the influences of non-optimal illumination, particularly at the studied site, a

minimum of seven single acquisitions is required. Sharpening the neodymium absorption band allows for robust mapping, even at the outer zones of enrichment. From the geochemical investigations, we found that iron oxides decrease the applicability of the method. However, iron-related absorption bands can be used as secondary indicators for sulfidic ore zones that are mainly enriched with rare earth elements. In summary, we found that hyperspectral spectroscopy is a noninvasive, fast and cost-saving method for determining neodymium at outcrop surfaces.

Keywords: rare earth elements; imaging spectroscopy; neodymium; hyperspectral; HySpex; remote sensing; Fen complex

1. Introduction

Today, rare earth elements (REE) are of special interest for the global economy. Particularly, REEs are important in modern technologies, such as batteries, LCD displays, catalytic converters, and in green technologies, such as wind turbines. Rare earth metals include the chemical elements of lanthanides. Scandium and yttrium are often grouped together with the rare earth metals because both elements have similar chemical properties and frequently occur in the same deposits. Detecting possible future deposits and determining the concentrations and relative enrichment of REEs in carbonatites, silicocarbonatites, peralkaline granites and pegmatites are of interest for mineral exploration and mining processes. The world's largest REE deposits are mostly bound to carbonatites or their altered equivalents [1]. The geochemical investigation of REE distributions within outcrops and the characterization of parental melts are currently debated and are usually performed by conducing laboratory analyses or by collecting handheld X-ray fluorescence measurements at a single spot [2]. Here, we present a new method that uses a hyperspectral imaging spectrometer (HySpex camera) for mapping the distribution of neodymium at the surface of a carbonatite outcrop in southern Norway. Generally, hyperspectral imagers can be applied from micro (laboratory) to macro (airborne or spaceborne systems) scales. Moreover, hyperspectral imaging is an ideal technology for monitoring exploration, particularly for reducing the environmental impacts of mining and decreasing costs. This study focuses on characterizing the REE distribution at one outcrop from one type of carbonatitic REE deposit by using the HySpex imaging spectrometer system.

1.1. Introduction to Hyperspectral Data Acquisition

A hyperspectral sensor uses the photoelectric effect by collecting pairs of free electron holes in the detector element. The number of collected electrons is a function of the incident photons. Thus, the function of illumination is determined in the radiometric calibration process for each detector element [3]. Hyperspectral sensors can be classified as either imaging spectrometers (e.g., HySpex) or point spectrometers (e.g., ASD field spectrometer). Single point spectrometers measure the incident electromagnetic radiation within a solid angle, whereas imaging spectrometers (in this case, a push broom line scanner) consist of at least one detector array and detectors that are contemporarily illuminated by spectrally and spatially dispersed incident electromagnetic radiation. Hence, each detector

element "counts" photons from a solid angle across a specific wavelength range and the system is configured to enable continuous spatial and spectral acquisition. If the detector array or the scanning object is moved over time and space, each scan line of a hyperspectral image represents one time step with a certain integration time, which can be used to successively collect the hyperspectral data cube. The x-axis of a hyperspectral data cube represents the number of detectors (across-track), the y-axis represents the number of frames or time steps (along-track) and the z-axis represents the wavelengths (spectrum). Thus, each pixel represents a single spectrum that can be analyzed to retrieve information regarding geochemical properties. Depending on the sensor, between 100 and 10,000 different wavelength ranges (bands) can be recorded on the z-axis. Minerals, metals and organic materials absorb electromagnetic radiation differently according to their inner structure and chemical composition. This absorption is detected as concave indentations within the spectrum that are referred to as absorption features. The position of the peak is referred to as the absorption band. Technically, different ranges of the electromagnetic spectrum represent different materials. Most absorption in the visible, near infrared (VNIR: 350 nm–1000 nm) and shortwave infrared (SWIR: 1000 nm–2500 nm) ranges can be explained by vibrational overtones, electronic transitions, charge transfer and/or conduction processes [4].

1.2. Introduction to Imaging Spectroscopy Principles for the Classification of Rare Earth Element Bearing Minerals and Rocks

In addition to the public spectral library of the USGS [4], the reflectance spectra of different minerals and rocks and spectroscopic investigations of carbonatite rocks have been published [5–11]. Generally, classification applications utilize spectrum-matching techniques that compare unknown spectra with known spectra from spectral libraries (Cross-correlations, spectral angle mapper, support vector machines, spectral feature fitting, *etc.*) [12,13] and spectral unmixing algorithms (linear spectral unmixing, pixel purity index) [12,13]. All of these methods are usually applied across the entire spectrum. Absorption features that are widely used to characterize mineral deposits include clay minerals (approximately 2.2 μm), calcite (approximately 2.33 μm), dolomite (approximately 2.34 μm) and iron oxides (approximately 900 nm, 650 nm and 540 nm) [4,12–15]. All of these absorption features are considerably broad, and the most mineralogically important bands are located in the SWIR. Exceptions include the characteristic absorption bands of metal oxides, such as iron oxides, and most of the REEs. According to Rowan *et al.* 1986 [5] and White 1967 [16], the absorption bands of REEs can be physically and chemically explained by electronic field transitions. This goes back to the fact that the 4f orbitals are partially occupied in nearly all lanthanides [17]. Overall, two electrons can occupy 7f orbitals, resulting in 14 different electron configurations. Except for lanthanum and lutetium, which have f orbitals that are completely occupied or empty, incident electromagnetic radiation will be absorbed at the appropriate energy, which results in electron excitations. This absorption is mainly detectable in the ultraviolet, visible, and near infrared ranges [5,16,17]. For example, the peak positions of the key spectral characteristic absorption bands for neodymium are ~580 nm, ~740 nm, ~800 nm, and ~870 nm [5,6,8,16]. In the 1960s, various rare earth oxide and rare earth chloride spectra were published that show absorption features in the visible and near infrared ranges [16,17]. Moreover, less abundant and less pronounced absorptions occur in the SWIR, which are usually explained by vibrations in the crystal lattice or chemical bond lengths. It is unknown if this observation holds for absorptions in the SWIR range of REE bearing minerals.

Another special property of REE-related absorption bands is their narrow shape, with the concave feature having a width of approximately 60–80 nm [5] (Figure 1). Two example spectra are shown in Figure 1. The first spectrum is from a hyperspectral integration of sand sized monazite crystals. The second spectrum integrates the fresh surface of a rock sample from the studied test site (see Chapter 2). The monazite sand was provided by Dan Harlov (REE percentage: La_2O_3: 12.49, Ce_2O_3: 28.77, Pr_2O_3: 3.058, Nd_2O_3: 12.28, Sm_2O_3: 1.694, HREE < 1.6%) [18]. Due to the multiple absorption shapes of neodymium related absorption features when a high percentage of neodymium is present in the sample, we used a natural sample with a medium-high concentration to generate an example spectrum. In this study, the monazite sand provides a good basis for defining the peak positions of the features because multiple absorptions are not resolved with the used spectrometer. The spectra were measured using an Analytical Spectral Device (ASD) spectrometer [19] and by integrating a circular area with a diameter of approximately 2 cm. Each of the collected spectra represents a mean of 200 averaged ASD spectra. In both example spectra, the absorption bands at ~580 nm, ~740 nm, ~800 nm, and ~870 are resolved. These bands are attributed to neodymium based on the publications of [5,16,17,20–22].

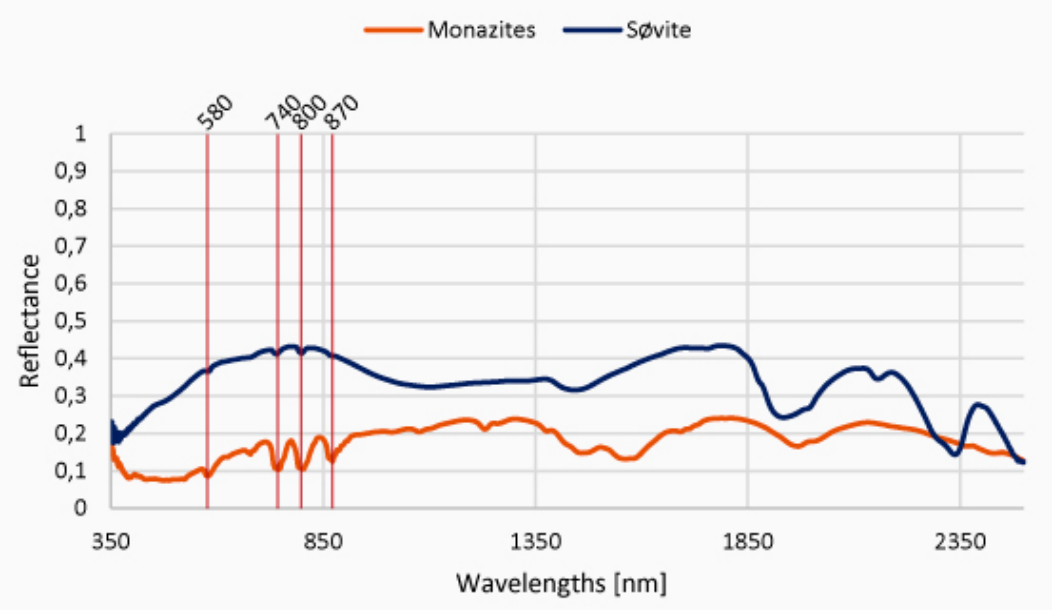

Figure 1. Two reference spectra for monazite (a neodymium-bearing mineral) and a monazite-rich rock sample (a calcitic carbonatite from the Fen complex). The key spectral characteristic absorption bands in the VNIR range that are associated with neodymium [5,16,17,20–22]. The graph is modified after Boesche *et al.* 2014 [23].

2. Geological Setting

The studied outcrop is located in an open cut natural mine located along Grønvoldvegen Road in Ulefoss, Nome, Norway (Figure 2) (location lat 59.282636°, lon 9.285511°). The outcrop consists of søvite type carbonatite rocks that are part of the Fen complex. This area was selected as the investigation area because it is widely recognized for its REE bearing igneous carbonate rocks. The Fen complex is formed from a Cambrian intrusion of alkaline and carbonatite melts that represent the volatile end fraction of a larger magma chamber, which probably lies beneath the surface [24–28]. Mitchell and Brunfeld [25] describe the søvites as a cap that lies on top of a urtite-ijolite-series (nepheline- and alkali-

pyroxene-rich intrusions). The final liquids represent the less abundant silicocarbonites. During this sequence of intrusion, fenitization of the country rocks occurred [25,27]. The silica-undersaturated magma provided a source of fenitizing fluids that altered the gneissic wall rocks, mainly to the west of the oval-shaped complex [27]. A second phase of intrusion occurred of damtjernite (ultramafic) composition that was later altered and metasomatized to alkaline magnesio-calcite carbonatites (rauhaugite) and ferro-carbonatites (rødbergite) [25].

Figure 2. Map of Norway showing the location of the study area and a ~180 degree image that was collected as part of the HySpex data acquisition. The two scale bars below the outcrop image indicate a distance of one meter horizontally and represent their exact vertical locations. The image is compressed towards the edges because the rotational acquisition mode was used. The overview map is modified after Boesche *et al.* 2014 [23].

3. Methods

3.1. Remote Sensing Analyses

3.1.1. Instruments and Fieldwork Procedure

The studied søvite outcrop (calcite carbonatites and silico-carbonatites) is located along a two-lane coastal road at lake Norsjø and strikes from the southeast to northwest. The surface normal to the outcrop points east. Therefore, solar illumination that is spectroscopically beneficial only occurs during the early morning hours. However, due to cloud formation in the early morning hours and because of the highest sun elevation (peak position was at *ca*. 1.30 p.m. in April), the best recording time was at ~2.00 p.m. The outcrop is approximately 50 m long with a height of approximately 6 m. The HySpex hyperspectral imager used in this study consists of two sensors (HySpex VNIR 1600/SWIR320 m-e), one operating in the visible and near infrared (VNIR: 350 nm–1000 nm) and the other operating in the shortwave infrared (SWIR: 1000 nm–2500 nm) [29]. These sensors were mounted on a tripod with a rotation stage and the entire system was installed *ca*. 10 m in front of the outcrop and perpendicular to the assumed REE enriched zones (Figure 3). High spatial resolution (pixel size) and low geometric distortion were achieved at the position of the REE enriched zone. The edges of the acquired images were always more distorted due to the rotational scanning process of the system, particularly because a field-of-view expander was used. The rotational acquisition was performed clockwise (from left to right), and a single acquisition period lasted for approximately two minutes, depending on the number of frames and the frame period. In this study, we only analyzed the VNIR image scene because most of the REE related absorption bands occurred within this specific range. The overall system settings are provided in Table 1.

The ground truth reflectance spectra of nine field samples (ground to a particle size < 63 μm) were obtained using an ASD Field spectrometer. We used a contact probe that was directly applied to the powdered samples to prevent stray light from superimposing the direct sample illumination and creating bias. Ground samples were used for these measurements because the ASD spectra were later compared with the chemical analyses results for the same sample powders.

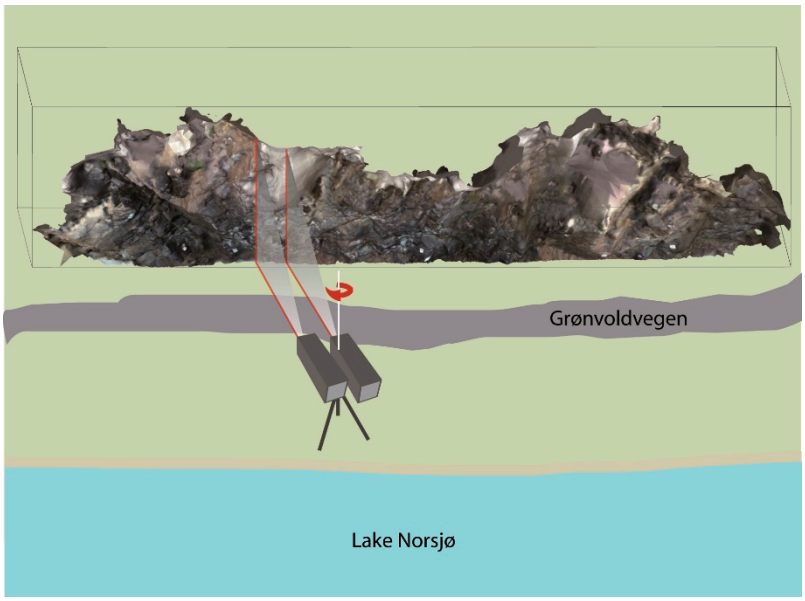

Figure 3. Experimental setup. The two HySpex cameras are located *ca*. 10 m in front of the outcrop. The measurement mode consisted of a clockwise rotation.

Table 1. Campaign settings for the two HySpex cameras. A high integration time was used because direct illumination was not present and due to the low reflectance targets.

Camera	VNIR	SWIR
Integration time (ms)	30	30
Frame period (ms)	31	61.753
Frames (#)	4000	1110
Field of view (°)	34 [1]	27 [1]
Spectral sampling interval (nm)	3.7	6
Radiometric resolution (bit)	12	14
Bands (#)	160	256
Detectors (pixel)	1600	320

[1] FOV is the Field Of View of the expander used to enable acquisition of nearly the full outcrop (height ~6 m in the VNIR, from a distance of 10 m).

3.1.2. Brief Description of the Proposed Approach

As shown in Figure 1, the REE related absorption features are so sharp that the spectral input of the entire spectrum would hamper the detection of small features within the matching algorithms due to the overestimation of the albedo and broad spectral signals (e.g., iron oxides). This result indicates the necessity of methods based on absorption bands, such as feature extraction [4] or modified Gaussian modeling [30]. These methods produce robust and reliable results for mineral mapping when the Signal-to-Noise Ratio

(SNR) is high, when only minor topographical variations exist, and when atmospheric scattering is low. Under fieldwork conditions, these criteria are unrealistic. In addition, other hampering factors must be considered. The identification of REE bearing minerals is, for example, aggravated when surfaces are partly covered (e.g., by vegetation and/or surface weathering) [31]. Additionally, atmospheric absorptions are spectrally adjacent to REE related absorptions, or even superimpose them. Absorption bands of atmospheric molecules have an unpredictable shape that depends on the atmospheric pressure and temperature and on different isotopes within the molecules and aerosols [32]. Consequently, the detection of small REE related absorption bands is complex. To overcome these difficulties, we combined two detection methods. First, a multitemporal approach is used to reduce noise and varying illumination due to the positions of clouds and the sun. The integration time used for image acquisition was determined by compromising between the duration of image acquisition and the signal-to-noise ratio. If the signal-to-noise ratio had increased when a longer integration time was used, the time difference between the first and last frame would have been longer than two minutes. Having an acquisition window of more than two minutes, effects such as sun azimuth changes, cloud movement and the movement of cars passing through the image potentially resulted in variations in the image quality. However, every nearly full-frame image was assigned for its homogeneity, and the best recording times at this particular location were determined. Next, the homogeneity parameters were used to obtain a weighted average of all scenes. Second (and afterwards), Richardson-Lucy deconvolution (R-L deconvolution), which is widely used to sharpen signals, was applied [33]. R-L deconvolution is performed according to the following principle. If absorptions are characterized by means of the albedo, all small but sharp absorption bands can be considered as high frequency contributions to the low frequency albedo signal according to signal processing theory. Thus, the wavelength dependent impulse noise would have a high frequency, and spectrally broad iron oxide absorptions would have a low frequency. Although a single absorption band only represents one oscillation, it is associated with a certain frequency. Hence, a full spectrum represents superimpositions of different frequencies that are located in certain ranges of the electromagnetic spectrum. Mathematically, R-L deconvolution is applied to enhance the spectral contrast for the frequencies that are related to REE absorptions. This specific high pass technique mainly sharpens absorptions, such as those from rare earth bearing minerals, and simultaneously preserves the shape of broader absorptions or the albedo. The absorption features have a shape that is similar to a Gaussian curve; thus, a Gaussian function was selected as a filter for R-L deconvolution. This function also addresses the assumption that the absorption bands represent a Gaussian distribution, regardless of the type of absorption (electronic field transitions or molecular motions) [34]. The definition of sigma for the Gaussian filter is a function of the desired REE absorption bands and must be selected beforehand. Here, the frequency of the Gaussian-shaped filter is twice the frequency of the smallest REE feature to avoid aliasing following the Nyquist Shannon theorem. The 70 nm wide neodymium feature that is the focus of this work can be observed in 18 VNIR HySpex channels. When the positive and negative 3σ interval (including 99.7% of the integral area) is equivalent to the filter width (here: 9 channels), sigma is calculated with a standard deviation of $\sigma = 1.5$.

3.1.3. Proposed Approach

Step 1 (Figure 4) is to collect multitemporal image scenes that must be transformed to reflectance data. For this study, five different reference panels are used for reflectance retrieval. These reference panels contain 5%, 20%, 50%, 90% and 95% calibrated reflectance standards and approximate the optimal Lambertian reflectance targets. Regarding the spatial shape of the outcrop, the 20% panel was mounted near the left edge of the outcrop, the 90% panel was mounted near the right edge of the outcrop and the 5%, 50% and 95% panels were mounted in the center with the normal surface of each panel oriented to the rotating sensor. The panels are measured during each acquisition to enable reflectance retrieval for each image. After measuring the raw Digital Number (DN), the data were radiometrically scaled to radiance ($W \cdot sr^{-1} \cdot m^{-2}$) by using radiometric calibration coefficients. Reflectance retrieval was performed by incorporating the panel-specific spectral and spatial averages. All panels were spatially delineated in each image set (an image set has the same acquisition properties). All pixel spectra for each panel were averaged to obtain mean panel spectra (as radiance) and successively normalized based on their reflectance level (e.g., 5%). A second order or greater order polynomial model was estimated for each image and band integrating all of the averaged and normalized panel spectra as gray values per band and image and their respective spatial position (pixel). Next, the polynomial model was inverted and applied pixel-wise to the image to retrieve the portion of incident radiation per image, band and pixel (irradiance). Next, this hyperspectral irradiance cube was used to normalize previously derived radiance values. Hence, reflectance retrieval was performed by rationing radiance to irradiance. After reflectance retrieval for each individual scene, a multitemporal average was generated by calculating a weighted mean of all single images. For this purpose, individual reflectance data cubes were evaluated with respect to the quality of each scene by analyzing the reference panels for spectral homogeneity. Spectral homogeneity was determined by calculating the standard deviations of all pixel spectra at the panel locations within the wavelength range where neodymium absorption features occur. The average for all scenes was calculated using a normalized weighting factor according to the spectral homogeneity as follows:

$$\overline{im} = \sum_i \frac{|\overline{WR} - WR_i|}{\sum_i |\overline{WR} - WR_i|} \cdot im_i \quad (1)$$

where *WR* represents all image pixels of the white references within the image scenes, *im* is the image scene and *i* is the running number of all collected images that are to be averaged.

In step 2 of this approach, each spectrum of the averaged image scene was smoothed using a Gaussian filter with the same sigma used for the R-L deconvolution to suppress the remaining noise. In addition, the spectrum was further transformed into relative absorption by using the following equation:

$$S = S(x, y, \lambda) = \log \frac{1}{\overline{im}(x, y, \lambda)} \quad (2)$$

where $S(x, y, \lambda)$ represents the smoothed absorption spectra of the averaged image scene (*im*). R-L deconvolution was conducted for every absorption spectrum $S(x, y, \lambda)$ following the principle that the Hadamard product of the Fourier transforms in the frequency domain equals convolution in the local domain. Here, the Hadamard product is the product of the initial image spectrum $S(x, y, \lambda)$ and the filter function (H), which provides the deconvolution term as follows:

$$S^{i+1} = S^i \circ H(x, y, \lambda) \tag{3}$$

$$H = H(x, y, \lambda) = \frac{\mathcal{F}\{S^0\}}{\mathcal{F}\{S^i * f\}} f \tag{4}$$

The input spectrum S^i is the spectrum of a single pixel (x, y) and is flipped upside down due to Equation (2). In addition, f is the filter function for R-L deconvolution and is the Gaussian distribution with a standard deviation σ = 1.5.

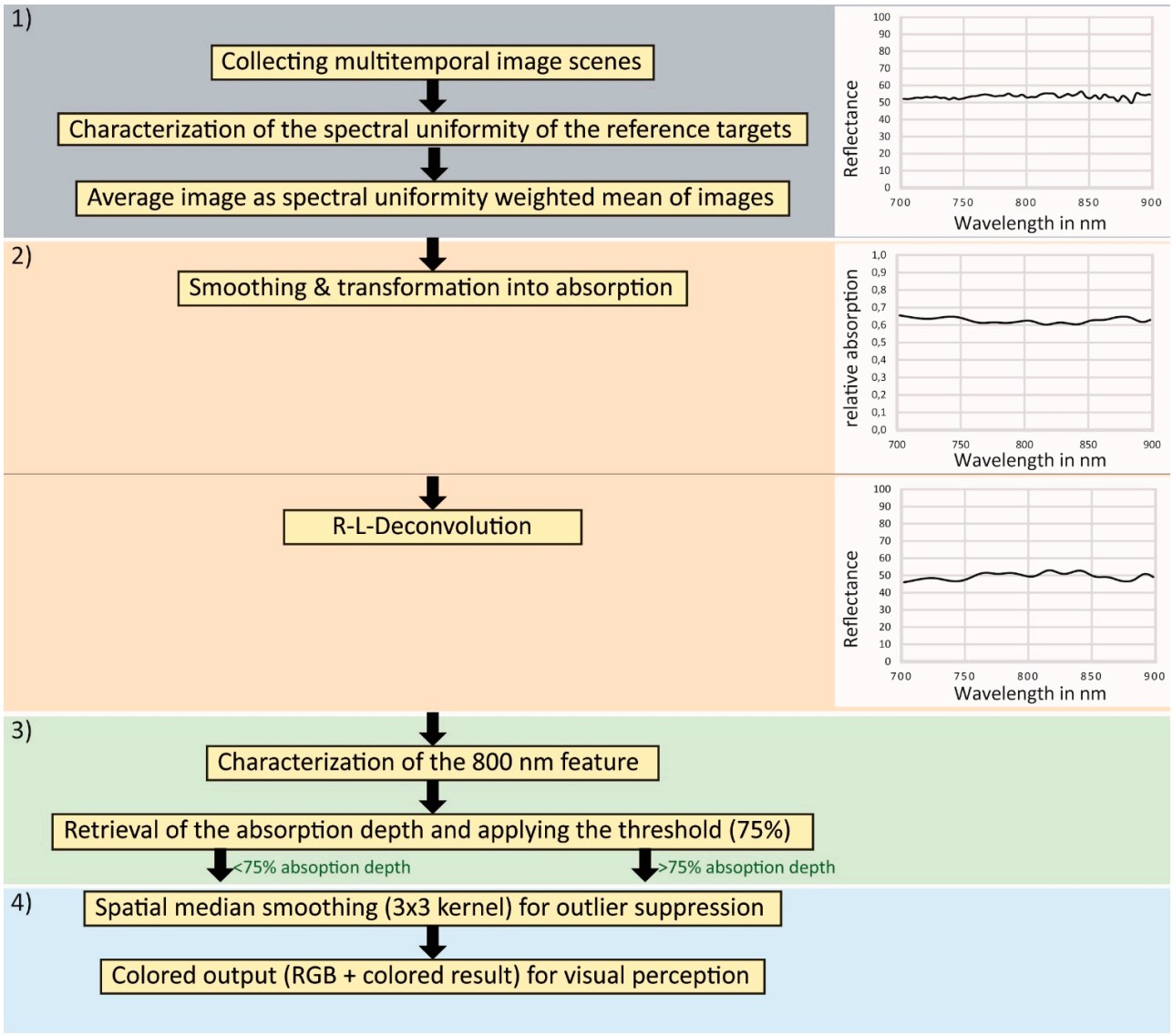

Figure 4. Flow Chart of the REE mapping approach showing the four main steps of its application. The first step is the collection of the multitemporal data cube and preprocessing. The second step is the application of Richardson-Lucy deconvolution. The third step is the identification and characterization of indicative and discriminative absorption bands and image pixel clustering. The fourth step describes the post-processing of the data and visualization.

In step 3, the spectra were exponentially transformed back to reflectance and the resulting spectra were directly used in the following steps to detect pixels that did or did not indicate REEs. The bands that were spectrally closest to the shoulders of the 800 nm neodymium feature were selected, and the

spectra between the shoulders were normalized using a straight line between the shoulders in a procedure known as continuum removal for features. After continuum normalization, the differences between the continuum and the peak of the absorption band were computed to retrieve the absorption depth. The peak of the absorption feature was determined precisely by resampling the reference spectrum from Figure 2 to the spectral channels of the HySpex imager (the 800 nm peak appeared at 803 nm). The positions of the two shoulders were determined using a continuum removal method (convex hull) for the down-sampled reference spectra. The left shoulder is at 778 nm and the right shoulder is at 840 nm. If the absorption depth of a pixel spectrum was higher than the three sigma of the noise (according to the averaged SNR) it was flagged as a REE indicative pixel. Step 4 includes outlier suppression using median filtering (here: 3 × 3 kernel) and coloring of the results.

3.2. Geochemical Analysis Tools for Retrieving Complimentary Information

3.2.1. Brief Theoretical Background of the Geochemical Methods and Sampling Design

The imaging spectroscopy methods delivered a high-resolution synopsis of the enriched and non-enriched areas of the surface of the outcrop. In addition, geochemical methods contribute to the exact quantitative compositional analyses of certain points. To obtain an overview of the REE distribution and further indications of the carbonatite-forming processes, several rock samples were collected along the outcrop. Their chemical and mineralogical compositions were analyzed from pulverized samples and thin sections thereby using three different methods. The first method was inductively coupled plasma atomic emission spectroscopy (ICP-AES), which was used to determine the REE concentrations of the pulverized samples. The second method was handheld X-ray fluorescence analysis of the same pulverized samples. The third method used an electron microprobe (EMPA) to characterize the composition of the REE-mineral monazite within thin sections. When validating the performance of the REE mapping method by geochemical analysis, it must be remembered that remote sensing techniques only penetrate the upper nm of the material. The surface penetration depth is wavelength dependent, and is half that of the center wavelength. Thus, remote sensing techniques can only determine the amounts of REEs within the weathered surface. Thus, it is important to sample thin chips (a few millimeters to one centimeter thick). In addition, if the samples contain too much fresh rock material, they must be cut parallel to the weathering surface and the fresh rock must be discarded. Because both positive and negative spectroscopic indications must be evaluated, rock samples were collected based on a preliminary image analysis using the 2.3 nm calcite feature and geologic field observations at the outcrop. These findings and the macroscopic analysis of the outcrop were used to identify sample locations (Figure 5). Generally, the outcrop was macroscopically divided into three rock units. The first unit consists of the carbonatite surrounding rocks of fenite, which mainly consist of silicate minerals (albite, potassic feldspar, quartz). The second and third rock units were established in schlieren and consist of melano-carbonatites (melanocrate minerals: biotite, iron oxides, pyrite, hornblende) and leuco-carbonatites (leucocrate minerals: carbonates, mica). Samples of these types of rocks were collected and were macroscopically determined to include REE-enriched carbonatites (HREE), medium REE-enriched carbonatites (MREE) and of less REE-enriched carbonatites (LREE). The geochemical results showed that samples 7L and 8L were not macroscopically classified in the field and actually were highly enriched samples.

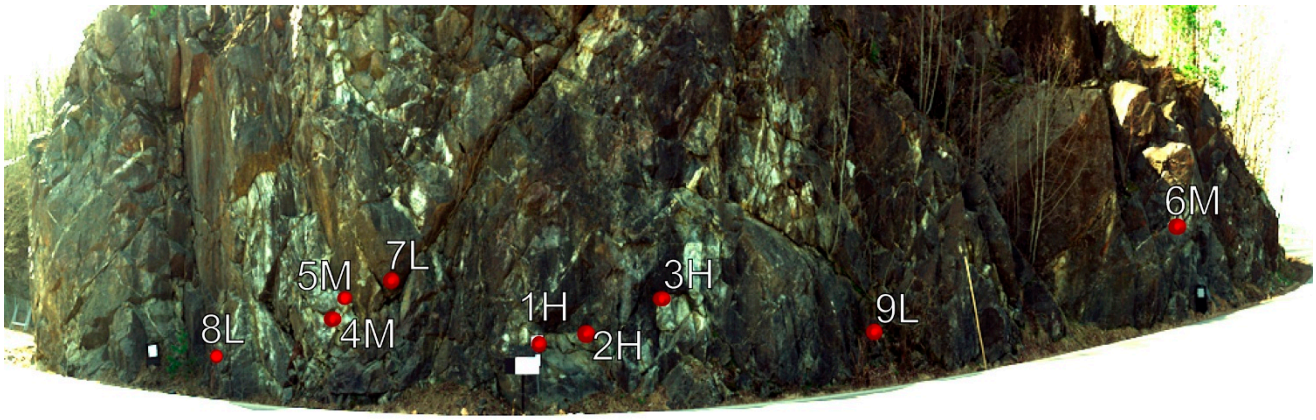

Figure 5. Sampling positions of the nine collected field samples. The letters within the descriptions of the sample locations represent the *in situ* interpretations of the relative sample enrichment (H-high, M-middle, L-low).

3.2.2. Realization and Instrumentation for Chemical Analysis

To validate the spectroscopic results, four geochemical analyses were conducted. Three methods were used to determine the elemental compositions of the field samples (see Section 3.2.1). The fourth method involved an analysis of the spectral behaviors of different artificial mixtures of neodymium and calcite carbonate.

When used on the field samples, the first method was helpful for determining the REE concentration. Nine rock samples were ground to a particle size of less than 63 µm. After sample preparation, chromatographic separation was applied using a Na_2O_2 sinter dissolution procedure before ion-exchange separation [35]. Then, geochemical analyses were performed using ICP-AES [35]. All results were normalized to C1-chondrite [36].

The second method was used to determine the major elemental abundances of rock samples and all other elements that could not be detected using ICP-AES. To accomplish this, the powder from the first method was further analyzed by using a handheld XRF instrument (Thermo Niton XL3) [37].

The third method included the mineral analysis of thin sections by using an electron microprobe (EMPA). The rock samples were cut into slabs to produce polished thin sections with a thickness of 30 µm that were coated with a layer of carbon. The thin sections were analyzed to determine the elemental compositions of the different monazite crystals by using a stationary electron microprobe (SuperProbe Jeol JXA–8230) [38].

The fourth method was used to estimate the extent at which the collection of hyperspectral images from the outcrop could be used to quantitatively determine the REE contents. Therefore, a series of artificial mixtures was measured in the laboratory and compared with the hyperspectral field recordings. For this purpose, certain amounts of neodymium oxide were mixed with calcium carbonate. The neodymium and calcium carbonate powders both had grain sizes of less than 63 µm. The investigated neodymium oxide percentages were approximately 0.1%, 0.5%, 1.0%, 2.0% and 5.0%. The exact concentrations were achieved using a precision digital scale. All mixtures were spectroscopically measured using the HySpex hyperspectral imager in the laboratory and their absorption depths at 803 nm were determined. As described in the chapter regarding the proposed method, the absorption depth was achieved by subtracting the reflectance value of the absorption band from the corresponding value at the feature-based continuum.

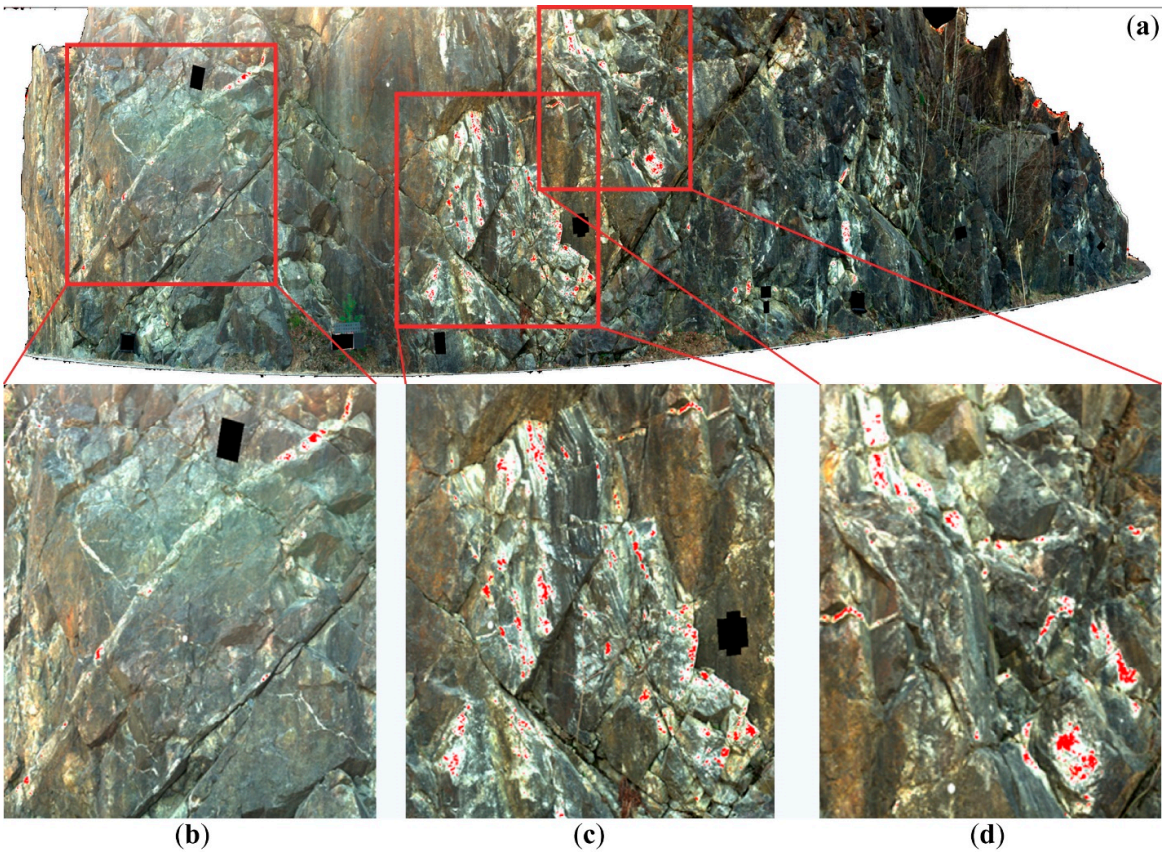

Figure 6. (**a**) REE thematic map of the søvite outcrop based on R-L deconvolution and combined with absorption depth determination. Red pixels indicate the enriched portion of the outcrop; (**b**–**d**) are the zoom images of the most important zones. Reference panels and the ground control points (for georeferencing) are colored black. The image highlights the local neodymium distribution as an indicator for LREE. The center area (c,d) is especially enriched in neodymium within the surface material that spatially follows the structured bands of alternating white and bluish weathering surfaces. Moreover, a ca. 4 m long band can be observed on the left portion of the outcrop (b) that is partly identified as containing neodymium oxide. Modified after Boesche *et al.* 2014 [23].

4. Results

4.1. Spectroscopy

The results of the proposed method include a thematic map that highlights the positively identified neodymium pixels in red (Figure 6). The reference panels and ground control points are covered in black. From the first *in situ* macroscopic descriptions and discrete spectroscopic measurements (ASD field spectrometer), areas of potentially high and low neodymium concentrations were identified. These zones are visible as whitish zones that were identified as leuco-carbonatites, bluish to light-brown zones of silico-carbonatites and silicate rocks (fenites) and brownish zones of melano-carbonatites according to geochemical testing. The hyperspectral mapping results from the introduced approach successively confirmed the presence of neodymium-enriched carbonatites (Figure 6). Particularly, one important finding is that the outer regions of the neodymium-enriched zones (transition zones from highly enriched

rocks to less concentrated ore zones) are still recognized. Thus, the zones with different compositions can be mapped better, including their gradual decrease in the direction of the outer contact zone (Figure 6a). In addition, REE containing pixels could still be identified when covered with a very small weathering layer or thin, small-scale vegetation layer (e.g., tiny lichens). At points with dense vegetation cover, soil forming on the top of the protruding morphology or a dense weathering surface, continuous positive detection was not possible because iron coatings hamper the detection of any underlying materials [15]. In addition, the remaining individual positive findings (1 to 4 adjacent pixels) were mostly deleted by the median filter. Melano-carbonatites are one example of a weathered rock and are brownish in color due to iron oxide coatings. The upper right corner in Figure 6 shows false positive identifications. The most plausible explanation for these false positives is the presence of transmissions from the leaves of small plants (moss, young plants and grass) growing on the outcrop.

4.2. Chemistry and Mineralogy

Compared with the REE distribution pattern published in [39], the distribution diagrams that were obtained for the ground truth samples (ICP-AES) show two different types of REE distributions (Figure 7). Although one distribution type represents rock types that consist of pure calcite-carbonatites (Figure 7a,b), the second type consists of siderite-bearing carbonatites (Figure 7c). The first type of distribution is represented by samples 1H, 2H, 3H, 4M, 5M, 6M and 9L and corresponds with the REE distributions published in Hornig-Kjarsgaard 1998 [39]. The second type of distribution is represented by samples 7L and 8L and shows a trend for the LREE that has been published for sulfide bearing søvites in Phalaborwa, South Africa [39]. In contrast with the steep slope towards the HREE in the Phalaborwa samples [39], the analyzed Fen samples plateau towards the HREE. All samples show a positive $(La/Lu)_{(n)}$ ratio that ranges from 30 in the first group to 170 in the second group (*i.e.*, siderite-bearing carbonatites) (Figure 7, Table 2).

The highest LREE concentrations (La, Ce, Pr, Nd, Sm) within the first type (calcite-carbonatite) were obtained for sample 6M, with a concentration of approximately 860 ppm, and for sample 5M, with a concentration of approximately 1270 ppm. The second type (siderite-bearing carbonatite) shows high concentrations of the middle REEs (Eu, Gd, Tb, Dy). Compared with the first rock type (*ca*. 40 ppm MREE in total), the second rock type contains up to 290 ppm MREE with a total LREE of up to 1900 ppm.

The handheld XRF measurements show the main differences between the two types of iron and the sulfur contents (see Table 3). In addition, pyrite was also visible in the hand specimen and on the outcrop surfaces.

The microscale analyses for both rock types showed evenly distributed rare earth minerals (mainly Ce-monazites and parisites; Table 4) within a matrix of calcite and some allanite. The monazites and parisites appear to represent different stages of fractionation evolution or epigenetic hydrothermal overprint. Few Ti-rich Fe-columbites occur. The ore rocks are sporadically veined. Some parisites include thorite or uraninite. Minor mineral occurrences of hematite needles, apatites, pyrites, ilmenites and barytes are present. The average composition of the monazites is provided in Table 4.

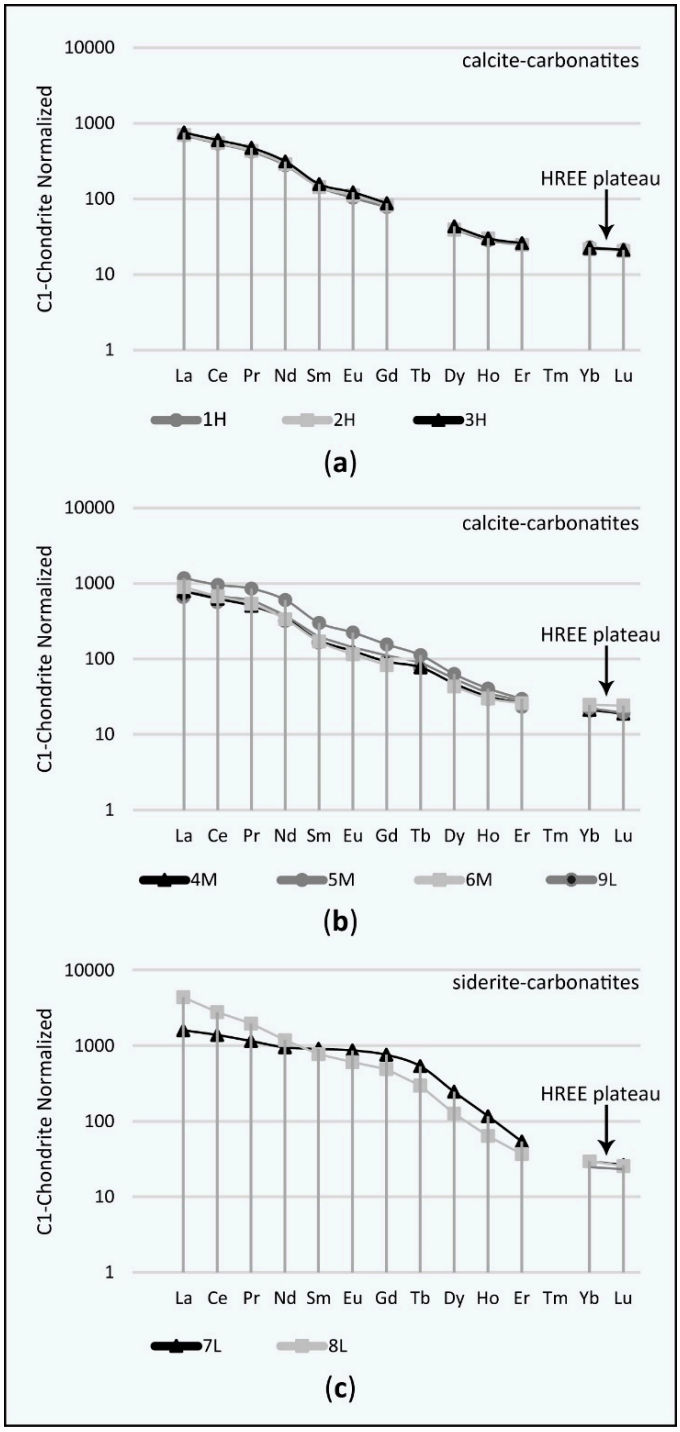

Figure 7. REE distribution patterns of nine collected field samples. The values are normalized to C1-chondrite [36]. Graph (**a**) shows the REE distribution patterns of samples 1H, 2H and 3H that were expected for the søvite outcrop, as published by [39]; Graph (**b**) shows four REE distributions of samples 4M, 5M, 6M, and 9L that mainly belong to the calcite-carbonatite rocks shown in graph (a). Sample 5M shows a slightly higher enrichment of light REE ($LREE_{(n)}$) and middle REE ($MREE_{(n)}$), but with the same distribution patterns as those for the samples in graph (a); Graph (**c**) shows different distributions that represent siderite-bearing carbonatites (7L and 8L) and indicates higher $LREE_{(n)}$ and $MREE_{(n)}$ concentrations. However, the $MREE_{(n)}$ indicates a positive anomaly. The curves plateau towards the heavy REEs ($HREE_{(n)}$) in all three graphs.

Table 2. Concentrations of REEs in the nine ground samples (ppm) and the C1-chondrite normalizing factors. Cerium (Ce) and gadolinium (Gd) show the differences between the two classes of rocks. Cerium represents the distribution of the LREE and gadolinium represents enrichment within the MREEs in samples 7L and 8L. N/A are either values that are not provided in the cited literature or are erroneous ICP-AES measurements.

	C1-Chondrite	1H	2H	3H	4M	5M	6M	7L	8L	9L
Y	N/A	48	49	51	53	61	50	168	89	58
La	0.237	164	167	179	186	278	212	377	1032	186
Ce	0.612	330	338	367	383	587	413	845	1699	413
Pr	0.095	40	41	45	48	81	51	109	185	58
Nd	0.467	130	135	146	161	282	157	442	550	178
Sm	0.153	22	22	24	27	46	26	138	118	30
Eu	0.058	6	6.5	7.1	7.4	13	6.7	50	35	8.3
Gd	0.2055	16	17	18	19	32	17	155	100	23
Tb	0.0374	N/A	N/A	N/A	2.9	4.2	N/A	20	11	3.4
Dy	0.254	10	10	11	12	16	11	62	32	14
Ho	0.0566	1.6	1.7	1.7	1.8	2.3	1.7	6.6	3.6	2.0
Er	0.1655	4.1	4.1	4.3	4.3	4.9	4.3	8.9	6.1	4.6
Tm	0.0255	N/A	N/A	N/A	N/A	N/A	N/A	N/A	N/A	N/A
Yb	0.17	3.9	3.7	3.8	3.6	3.8	4.2	5.0	5.0	4.2
Lu	0.0254	0.54	0.52	0.54	0.48	0.49	0.61	0.67	0.65	0.59
Sc	N/A	2.2	2	3.6	2.1	2.9	3.7	74	33	5.3

Table 3. Elemental compositions of nine ground field samples analyzed using the handheld XRF. All samples had calcium concentrations of between *ca*. 35% and 45%. The lower calcium concentrations were observed in samples 7L and 8L. These two samples also had higher concentrations of iron, yttrium, thorium and uranium. However, all samples can be subdivided into pure calcium carbonatites (1H, 2H, 3H, 4M, 5M, 6M and 9L) and the two siderite bearing carbonatite samples enriched with Th, U, Y and REEs (7L and 8L). LOD represents the limit of detection.

Reading No.	1H	2H	3H	4M	5M	6M	7L	8L	9L
Duration of measurement (s)	122.79	124.86	132.57	123.58	121.99	120.58	124.35	123.32	123.38
Units	ppm	ppm	ppm	ppm	ppm	ppm	ppm	ppm	ppm
Nb	2493.48	1155.47	1694.60	2094.15	2963.61	521.13	4748.08	1578.00	1447.73
Y	62.31	59.15	58.60	63.69	71.98	58.74	176.11	111.74	64.98
Th	<LOD	<LOD	<LOD	<LOD	<LOD	<LOD	<LOD	480.00	<LOD
U	<LOD	<LOD	<LOD	<LOD	<LOD	<LOD	121.81	<LOD	<LOD
Units	percent	percent	percent	percent	percent	percent	percent	percent	percent
Fe	0.64	0.26	0.38	0.29	0.67	0.38	3.87	4.50	0.84
Ca	43.35	43.24	43.33	43.69	41.39	43.29	32.32	36.23	42.56
K	0.16	0.06	0.12	<LOD	0.09	<LOD	0.13	0.09	0.06
S	0.13	<LOD	<LOD	<LOD	0.08	<LOD	0.44	1.05	0.23

Table 3. *Cont.*

Reading No.	1H	2H	3H	4M	5M	6M	7L	8L	9L
P	0.24	0.34	0.55	0.70	2.46	0.20	1.03	0.41	0.44
Si	1.03	0.66	1.25	0.44	1.03	0.43	1.17	0.81	0.77
Cl	0.01	0.01	0.01	<LOD	0.01	0.01	0.01	0.01	0.02
Mn	0.31	0.24	0.35	0.26	0.43	0.47	0.54	0.42	0.36
Al	<LOD	<LOD	<LOD	<LOD	<LOD	<LOD	<LOD	<LOD	<LOD
Mg	<LOD	<LOD	<LOD	<LOD	<LOD	<LOD	<LOD	<LOD	<LOD
Not detectable	52.91	53.99	52.72	53.53	52.67	54.28	57.42	54.99	53.98
Total	99.21	99.10	99.04	99.33	99.40	99.29	97.75	99.12	99.52

Table 4. Averaged elemental concentrations of 19 individual monazite crystals. All monazites are pure calcium carbonatite rocks, and due to the high amounts of cerium, all monazites are Ce-monazites. The presented values were determined by using electron microprobe analyses.

Element Oxide	Average Weight Percent of 19 Monazite Measurements
P2O5	30.05
CaO	0.79
SiO2	0.35
Al2O3	0.04
FeO	0.36
Y2O3	0.12
La2O3	12.98
Ce2O3	31.83
Nd2O3	15.61
Pr2O3	4.00
Sm2O3	1.81
Gd2O3	0.60
Tb2O3	0.03
Dy2O3	0.08
Ho2O3	0.01
Er2O3	0.03
Yb2O3	0.01
Lu2O3	<LOD
ThO2	0.22
UO2	<LOD
PbO	0.02
Total	98.94

5. Discussion

5.1. Validation of the Proposed Method, the Richardson Lucy Deconvolution and the Multitemporal Approach

To discuss the benefits of R-L deconvolution, the results from only using the absorption band depth determination method and the results from after applying R-L deconvolution were compared. Many absorption bands were not identified until deconvolution strengthened them and made them detectable.

Figures 8 and 9 show that detection using R-L deconvolution was beneficial, especially for transitional zones with less prominent features. The graphs in Figure 8 show four different spectra of pixels that are good examples for different neodymium concentrations at the outcrop and are verified by geochemical sample analysis (sample position 1H, Figure 5). The straight line in each spectrum shows the continuum of the feature that was anchored at the shoulders of the 803 nm feature. The value in the legend indicates the absorption depth (which is the difference between the absorption band at 803 nm and the corresponding value of the continuum). Negative values represent non-enriched pixels because no defined absorption bands are mathematically describable. The yellow spectrum is extracted at the center of the ore zone and the red spectrum is extracted at the wall rocks of the carbonatite. The pixels that mark the transition between the ore zone and the wall rocks of the carbonatite are represented by orange and green spectra. The difference between the simple absorption depth determination and the determination of absorption depth is especially visible for those pixels after applying the introduced deconvolution approach. While the orange and yellow spectra can still be described with an absorption feature at 803 nm in both graphs, the green spectrum of the simple approach did not show any absorption features until after R-L deconvolution was applied. Thus, the introduced approach was helpful for more accurately delineating the borders of enriched zones. Figure 9 shows the final mapping results of the outcrop without using the introduced approach and compares the zoom images with those shown in Figure 6.

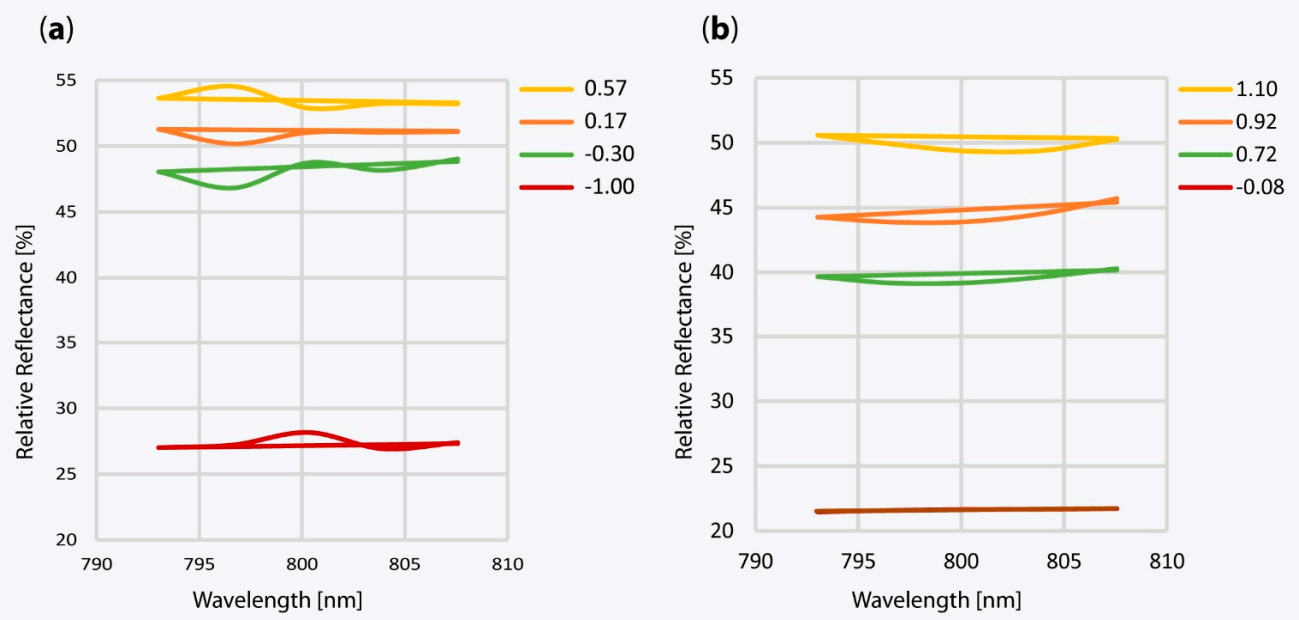

Figure 8. A comparison between four image spectra with and without applying R-L deconvolution. (**a**) Image spectra from the simple run (without R-L deconvolution); and (**b**) image spectra from the full approach (including R-L deconvolution). The legend values represent the absorption depth (difference between the absorption band at 803 nm and its corresponding value in the continuum). Deconvolution has a high potential for mapping the exact borders of these zones, especially for transition pixels at the outer zones of the REE-enriched parts. Modified after Boesche *et al.* 2014 [23].

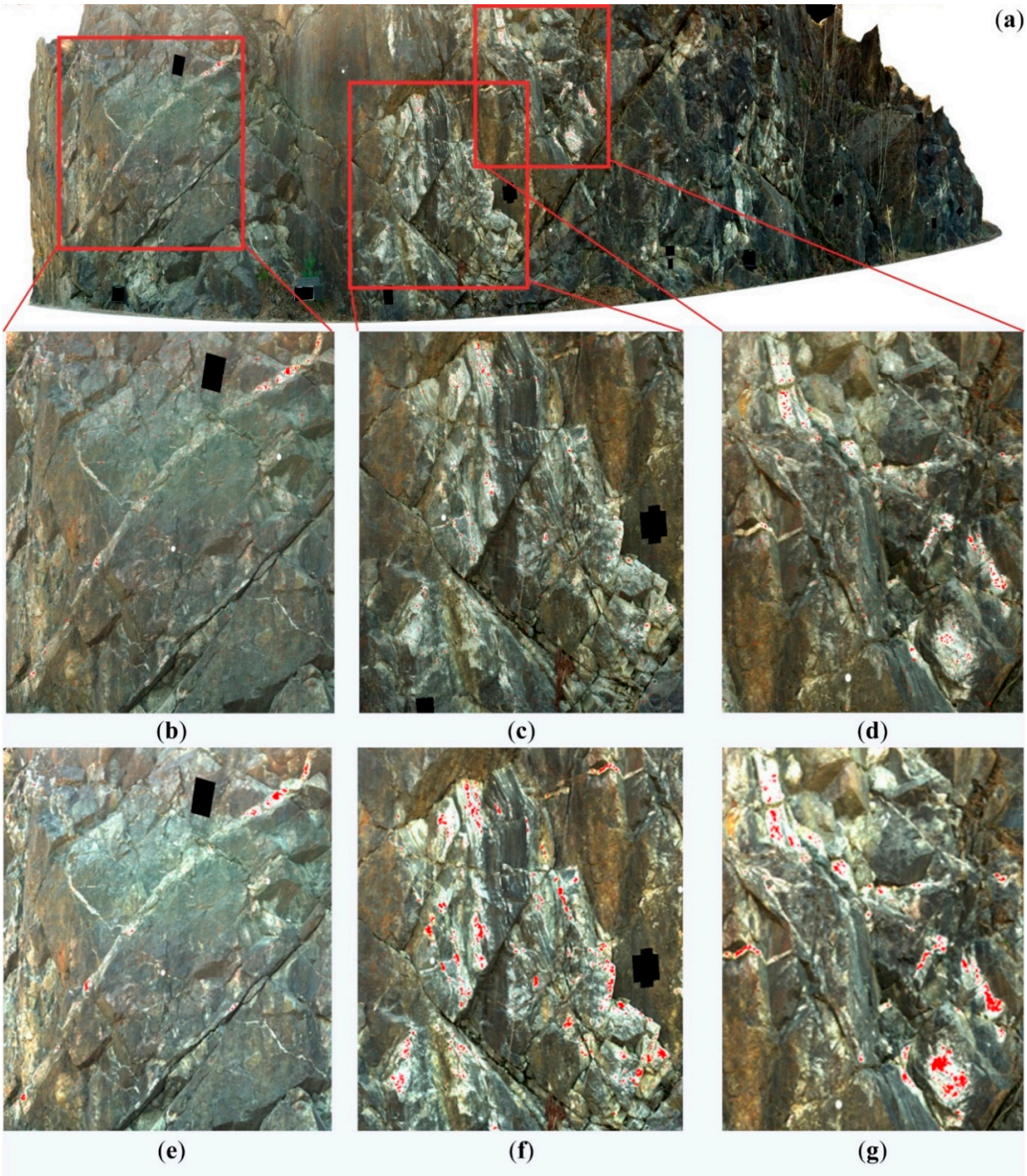

Figure 9. REE thematic map based on the simple algorithm (without R-L deconvolution). Enriched zones cannot be identified at their full spatial extent. (**a**) Shows the full extent of the map; (**b**–**d**) are zoom images at where the original approach shows the most positive findings. Here, only some pixels could be identified correctly. For comparison, the results of the full approach shown in Figure 6b–d are shown in the zoom images (**e**–**g**). Modified after Boesche *et al.* 2014 [23].

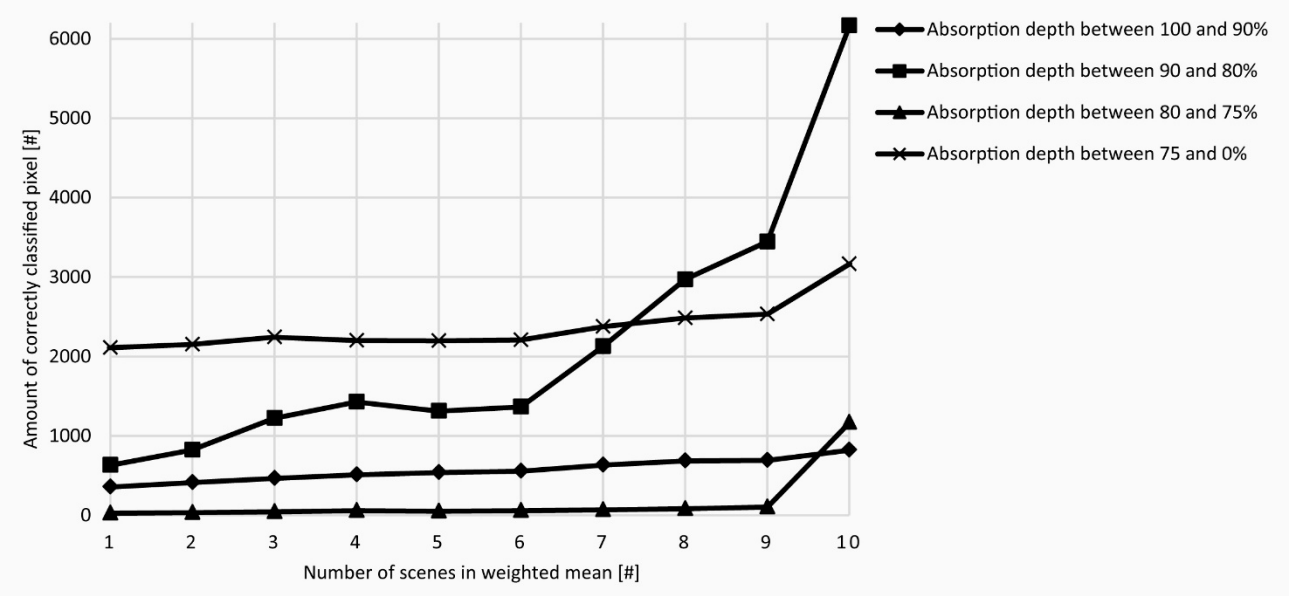

Figure 10. The impacts of using multiple image scenes for a weighted mean in the first step of the approach. Each run was performed using one more of the collected image scenes. The first run was accomplished using the image scene with the highest homogeneity for the white references. The SNR was calculated using the reference panels that were placed in front of the outcrop. Run after run, one image scene was added to the weighted mean according to its descending SNR. After using the best seven scenes, an increase in the number of correctly classified pixels was observed for the transition pixels between the enriched zones and the unenriched areas. From then on, every run that included one additional scene had a better result.

Regarding the low image SNR, several image collections were taken using a multitemporal approach. Ten images were necessary for obtaining a good quality average. To determine the minimum number of images required for the first, quick REE detection and the number of images required for a high-quality product, all scenes were sorted with respect to reflectance panel homogeneity. Then, for each run of the introduced approach, each of the sorted images was added individually in descending order of their homogeneity. After every run, a REE thematic map was generated. After ten runs, all of the resulting maps were classified. To classify all of the indicative pixels for each resulting image into statistically significant quantiles (here four classes), the absorption depths of all spectra were scaled to values of 0 to 255, which is a broadly accepted 8-Bit image quantization technique for suppressing noisy outliers. Consequently, every image had the same maximum absorption value and scaling. To establish the four classes as quantiles of the abundance distribution, percentage values were used to improve the interpretability. The first class or 10-quantile comprises all pixels with spectra showing absorption depths of between 100% and 90% (255–230 absorption depth value). In addition, the second class or 10-quantile encompasses between 90% and 80% (230–204 absorption depth value), the third class or 5-quantile encompasses between 80% and 75% (204–190 absorption depth value), and the last class or 4-quartile represents the pixels that are below 75% (190 absorption depth value) or do not show a significant absorption band (0 to negative absorption depths). To compare the ten classification results with each other, we extracted a predefined region of interest that only covers the pixel that were flagged as neodymium enriched in the ten-fold weighted average image (11,343 pixel). Because the ten-fold

average likely provides the most reliable result, we assumed that all neodymium rich flagged pixels were correctly classified. Hence, the following comparison is restricted to the relative omission classification error when less than ten images were used. The commission error and the absolute omission error are not testable in this case because a dense grid of ground truth sampling (several hundred to be statistically accurate) was not possible in terms of the laboratory analysis periods for geochemical REE analysis. The results (Figure 10) show that the accuracy of the classification is not increasing linearly for all quantiles. Regarding the pixels that show strong features within the spectrum (absorption depths of between 90% and 100%), the number of correctly classified pixels does not change significantly as the number of averaged scenes increases (Figure 10). The same independence of the number of averaged scenes can be observed for non-indicative pixels. However, for pixels that mark the transition zone between carbonatite surrounding rocks and the ore zone (90% to 80%), the average number of scenes is very relevant. In this study, seven scenes were required to observe an increase in the neodymium detection accuracy within these transition zones. With each additional scene, a noticeable increase in accuracy was observed. Finally, the noise depends on many factors (weather, instrument characteristics, multiple reflections of surrounding objects (trees, buildings, cars, lakes, *etc.*)) that noise estimations would always count under specific measurement conditions. However, the question of how many scenes one would need under similar conditions to obtain an improved classification result could be answered.

5.2. Discussion of the Results from the Introduced New Method and their Chemical Evaluation

As described in the chemical analysis results, outcrop rock types can be divided into two different rock classes. Although both of the classes are carbonatites, one class contains more ore minerals (such as REE minerals, iron ores and pyrites). Figure 11 shows the laboratory reflectance spectra for all collected and powdered field samples that were measured using the ASD spectrometer. The pyrite bearing carbonatites are represented by the 7L and 8L spectra in orange and yellow (Figure 11). Both spectra show strong iron oxide features (that would superimpose the neodymium feature [15]) and a very small calcite absorption band. By contrast, the spectra of samples 4M and 6M, which contain medium enrichments of sulfates and REEs, show low iron absorption at 530 nm and 910 nm. However, the 670 nm feature is missing. These two features would not superimpose the 800 nm neodymium feature. Hence, these spectra provide robust results for spectral neodymium analysis. The zoom image in the lower right corner of Figure 11 shows a continuum-removed subset of the spectra that points towards the neodymium oxide absorption band at approximately 800 nm. The samples with the highest neodymium absorption are 5M, 2H and 6M. The absorption band at approximately 800 nm of sample 6M shows a shift towards shorter wavelength/higher energy. This shift may be explained by the higher amounts of bastnaesites or parisites in the ore rocks. In spectra from bastnaesite and parasite, the peak absorptions occur at 797 and 798 nm [22]. However, in monazites, the peak position occurs at 800 nm (Figure 1). The main differences between the chemical bonds of the Nd^{3+} in monazite and in the bastnaesite solid solution series is the presence of a fluorine atom in the bastnaesites series. It is broadly assumed that the absorption features for REEs can be explained by electronic field transitions [5,21,22] in the 4f-orbitals. The 4f-orbitals are shielded by the $5s^2$ and $5p^6$ orbitals. The inner location of the 4f-orbitals is believed to prevent 4f orbitals from influencing the orbitals of the host mineral [20]. However, shifts towards shorter wavelengths were observed and explained by Kumar *et al.* [21], who analyzed two different chalcogen bound Nd^{3+}

compounds, and by Misra *et al.* [40], who compared the absorption spectra of trifluoroacetate and trichloroacetate. Kumar *et al.* described the occurrence of a blue shift for the 800 nm feature ($^4I_{9/2} \rightarrow {}^4F_{5/2}$ shift: 801 nm to 797 nm [21]) for a material in which neodymium is surrounded by SC_6F_5. Misra *et al.* 2006 described the $^4F_{5/2}$ shift as ligand mediated pseudohypersensitive. Kumar *et al.* explained the hypersensitive transition shifts of absorption bands with changes in the covalency of the bond [21]. Whether this decrease results from fluorine atoms was not answered directly. However, the decrease in the polarizability (due to the high electronegativity) of the ligands (F) around Nd^{3+} is provided as an explanation for the decreased overlap of the ligand (F) and Nd^{3+} orbitals [21,40]. Further, Kumar *et al.* [21] explain the occurrence of an inverse proportionality between the shifts in peak-wavelength and the 4f–5d energy difference.

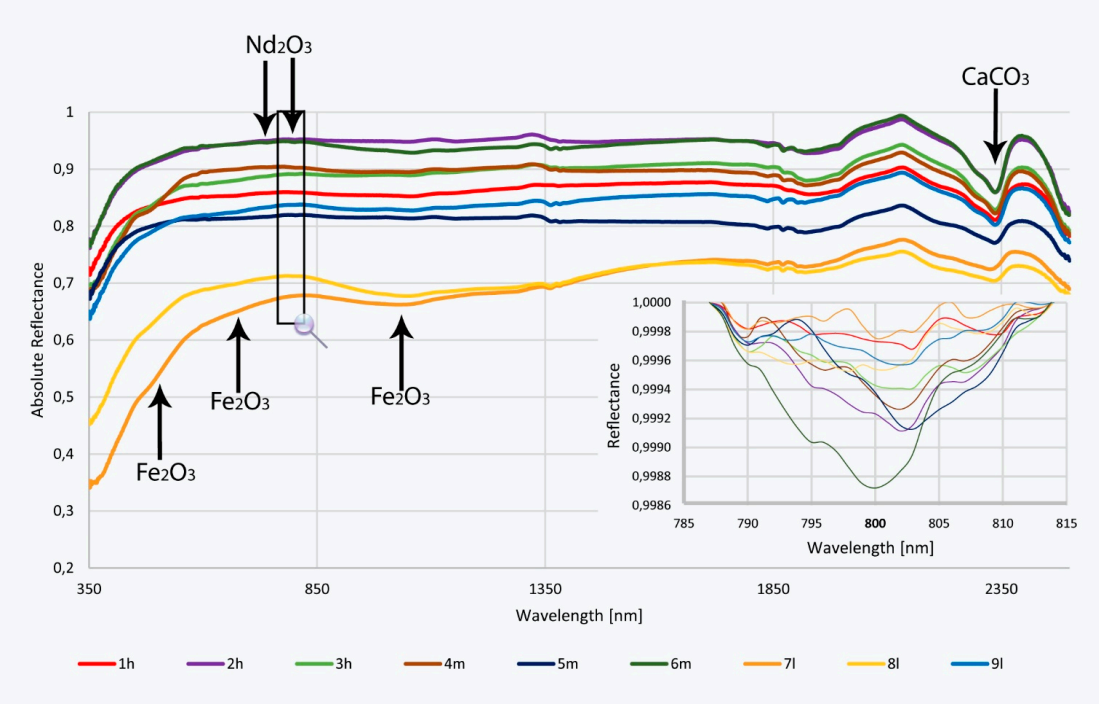

Figure 11. Resulting ASD spectra of the ground truth measurements. The zoom image shows (feature based) continuum-removed subsets of the ground truth measurements. The spectra of samples 1H, 2H, 3H, 4M, 5M, 6M and 9L show a nicely resolved calcium carbonate absorption band at 2.3 nm and a small superimposition of neodymium oxides. The spectra of samples 7L and 8L show less absorption for the calcium carbonate band. The two spectra clearly show three iron oxide absorption bands. Hence, the spectra are correlated with the chemical results in Tables 2 and 3. The 800 nm absorption band is the most diagnostic feature for neodymium detection. A correlation between the absorption depth and neodymium content is visible (especially for the spectra of samples 5M, 2H, 6M, 4M and 3H), if they contain no iron oxide.

A second explanation for this shift may be the higher amount of thulium, which absorbs at 801 nm and superimposes the neodymium absorption band [16]. Based on the geochemical analysis used in this study, it was not possible to validate the shift of the 800 nm feature with the exact concentrations of thulium in the rock samples. However, the distribution patterns shown in Figure 7 can be used as indicators

for the values of thulium when analyzing general trends of the HREE plateau. Hence, Figure 7b,c show higher HREE values in sample 6M compared with samples 1H, 2H, 3H, 4M, 5M and 9L, and lower values than samples 7L and 8L. The spectra of samples 7L and 8L would not show thulium absorption because of the iron content. Thus, sample 6M is the only spectrum that shows the superimposed and widened feature of neodymium and thulium.

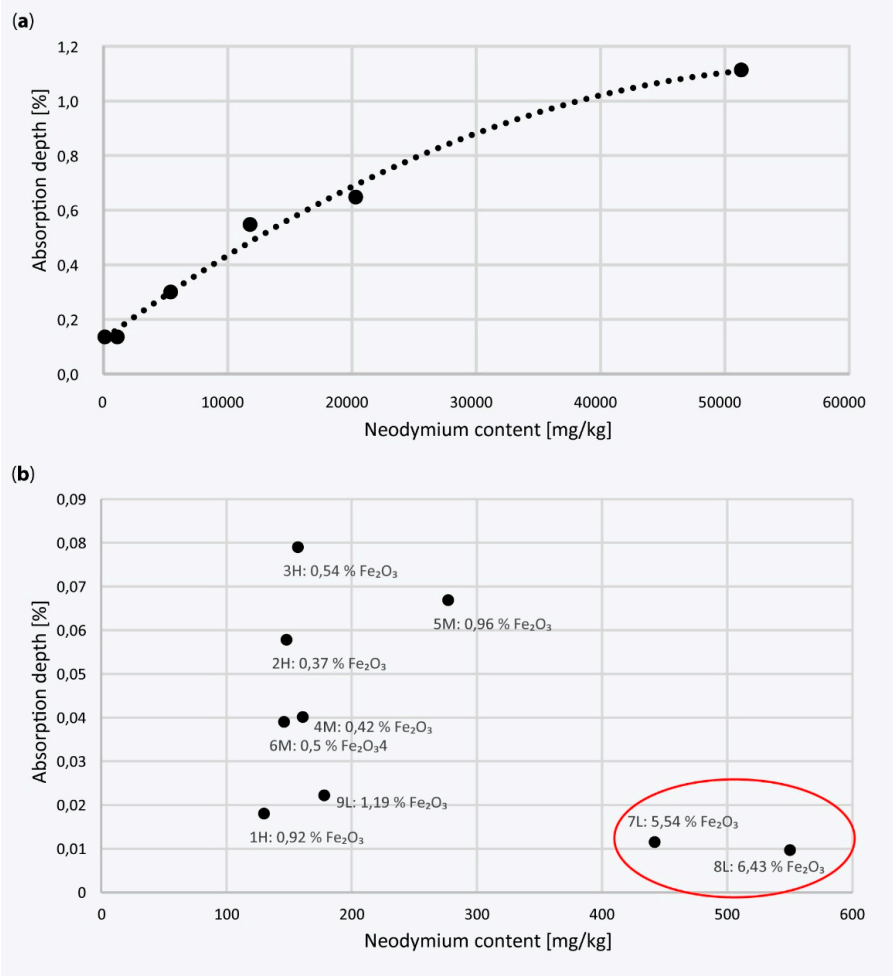

Figure 12. Quantitative comparison between the neodymium concentrations of mixture samples and field samples and the corresponding hyperspectral recordings. (**a**) Correlation between the amount of neodymium oxide within a calcium carbonate powder and the absorption depth of the 803 nm absorption band measured with the HySpex spectrometer in the laboratory. The trend line is a second-degree polynomial fit. (**b**) Correlation of the REE content of the field-samples with the depths of the neodymium absorption band measured with the ASD field spectrometer in the laboratory. Only samples 7L and 8L occur as outliers. This result is due to the iron oxide content, which is shown for all field samples as index numbers next to the plotted points in graph (b).

The quantitative concentration determination results of a series of laboratory measurements of artificial sample mixtures ($CaCO_3$ and Nd_2O_3) that were compared with hyperspectral recordings revealed an algebraic dependence between the 800 nm absorption band (Figure 12: y-axis) and the neodymium concentration (Figure 12: x-axis). Figure 12a shows that for the laboratory mixtures with minor

neodymium concentrations less than 5%, the two parameters are multiplicatively dependent with a polynomial grade of two. Figure 12b shows the neodymium concentration of the powdered field samples plotted on the x-axis and the absorption depths of the hyperspectral ASD measurements on the y-axis. In addition, Figure 12b shows that an algebraic dependency between the neodymium concentration and absorption depth may only be visible for samples with low pyrite. This observation is occurs because the very small amount of iron oxide (less than 10%) dramatically hampers the identification of REE related absorption bands (Figure 12b: values in the red circle). In addition, this observation can be explained by the fact that the presence of only minor concentrations of iron oxides (approximately 5%–6% FeO or Fe_2O_3) within the weathered surfaces of the rocks inhibits any reflection of the subsurface material. Additionally, [31] stated that a thin reddish film resulting from rubification processes (e.g., free iron oxides that were released from the rock and coat the surface of an outcrop) already exists and significantly affects the spectrum. Therefore, spectral muting in the presence of iron oxides makes identification of the small REE absorption bands impossible. A new study on how carbonatites erode and weather under Scandinavian climate conditions (rain, frost, snow, *etc.*) and on how mobile rare earth elements behave in the weathering surface is necessary for quantifying weathering as a hampering factor. Besides the pyrite rich samples, the algebraic dependency shows that spectroscopy has a large potential to semi-quantify low REE concentrations. However, superimpositions with other materials hamper direct quantitative estimations. To quantify the influences of vegetation coverage, the exact species, leaf thickness, the ability of the plant to store REEs in the fabrics of the roots or leaves and the multiple reflections and transmittance of the incident radiation at the vegetation pixel must be considered.

6. Conclusions

The results of our study provide valuable information regarding the concentrations and distributions of rare earth elements in carbonatites. The proposed approach is a first and robust tool for spectroscopically identifying rare earth elements. This approach allows for spatial mapping of distribution patterns at different enrichment levels and provides further insights regarding the signatures of the parental magma.

- Spectroscopy has been identified as a powerful tool for mapping outcrops for rare earth elements, even under nonoptimal illumination conditions (e.g., dark materials, shadowed outcrops, low sun elevation angles). Remarkable hyperspectral mapping of neodymium-enriched zones is achievable if data acquisition conditions are good or if multitemporal scenes are collected and the outcrop has little or no weathered surface.

- The R-L-deconvolution method has a high potential for resolving neodymium related absorption bands, even when the noise is considerably high.

- The weighted mean of a minimum of seven scenes already allows for good mapping of transition zones. To locate the highly enriched zones of the outcrop, only one scene taken under good illumination conditions is required.

- Our approach is suitable for analyzing outcrops that are located short distances from the sensor (30 m to 5 m). The presented approach provides results within a short period of ~10–30 min, including field measurements, and can be readily used in the field as an additional tool for mineral prospecting processes. We suggest applying this approach in a two-step procedure. The first step involves a run with a fast integration time and low multi-temporal average. This quick-result serves as a basis for setting up

the ideal acquisition conditions in the field (e.g., the position of the sensor, position of the white references, illumination angles). The second step includes the full approach with the best integration time and a high number of acquisitions.

- The spectroscopic results show a direct relationship between low-pyrite carbonatites and the geochemical results. Therefore, this approach produces accurate results when the iron content is low. Nevertheless, iron and other ore minerals can be used to detect enriched zones within the carbonatite body because higher amounts of iron ore minerals represent a secondary indicator of sulfidic conditions during melt intrusion and can highlight particularly enriched zones.

- The geochemical results show two classes of rock types within the investigated søvite outcrop. The first type (carbonatite) shows the expected rare earth element distribution, and the second type (siderite-carbonatite) contains surprisingly high amounts of the middle rare earth elements.

Future studies should focus on the key spectral characteristics of the remaining 15 rare earth elements. In addition, we recommend investigating the potential of iron oxide spectroscopy as a secondary indicator of sulfidic melts in carbonatitic rocks. Quantifying the applicability in the presence of spectroscopical hampering materials, such as vegetation or iron coatings, would be very interesting. Additional hampering factors, such as incidence angles, illumination angles, non-optimal acquisition conditions (lack of white references in the images, shifts of pixel due to the unstable underground of the tripod) and dust should be focused on in the future. Moreover, the proposed technique could be tested at different scales (e.g., microscopical image collections on thin sections and remote sensing of the whole ore body from airborne and space borne). Finally, the geological interpretation of carbonatitic outcrops might be enhanced by incorporating LiDAR or from photogrammically retrieved three-dimensional surface models to conduct more complex spatial analyses of the mineral phases in the outcrop. This method would be especially useful when using the REE mapping technique for vertical 3D monitoring of vertical open pit mining surfaces.

Acknowledgments

This study was financed and scientifically supported by the German National EnMAP framework program (Department of Economics and Technology BMWi No. 50EE1256) and the GeoForschungsZentrum (GFZ) of the Helmholtz Foundation. We would like to thank BERGFALD Miljørådgivere for significantly supporting our work and for allowing us to work at the Fen complex. Many thanks are extended to the editors and the reviewers for their valuable comments, which have helped improve the quality of this paper.

Author Contributions

Nina Kristine Bösche initiated and carried out this study and wrote the manuscript. Christian Rogaß helped with the preprocessing of the collected field data, including radiometric calibration and reflectance retrieval. Christin Lubitz, Christian Rogaß and Maximilian Brell belonged to the field excursion team and made successful image collections possible. Sabrina Herrmann conducted the laboratory measurements of the powdered samples and neodymium mixtures with the HySpex and handheld XRF instruments. Christian Mielke, Sabine Tonn and Oona Appelt monitored the geochemical analyses at the GFZ

laboratories. Uwe Altenberger and Hermann Kaufmann supervised this work and helped with the interpretation of the mineral analyses.

Conflicts of Interest

The authors declare no conflict of interest.

References

1. Laznicka, P. *Giant Metallic Deposits*; Springer Berlin Heidelberg: Berlin/Heidelberg, Germany, 2010.
2. Xu, C.; Wang, L.; Song, W.; Wu, M. Carbonatites in China: A review for genesis and mineralization. *Geosci. Front.* **2010**, *1*, 105–114.
3. Rogass, C.; Spengler, D.; Bochow, M.; Segl, K.; Lausch, A.; Doktor, D.; Roessner, S.; Behling, R.; Wetzel, H.U.; Kaufmann, H. Reduction of radiometric miscalibration—Applications to pushbroom sensors. *Sensors* **2011**, *11*, 6370–6395.
4. Clark, R.N.; Swayze, G.A.; Livo, K.E.; Kokaly, R.F.; Sutley, S.J.; Dalton, J.B.; McDougal, R.R.; Gent, C.A. Imaging spectroscopy: Earth and planetary remote sensing with the USGS Tetracorder and expert systems. *J. Geophys. Res.* **2003**, doi:10.1029/2002JE001847.
5. Rowan, L.C.; Kingston, M.J.; Crowley, J.K. Spectral reflectance of carbonatites and related alkalic igneous rocks; selected samples from four North American localities. *Econ. Geol.* **1986**, *81*, 857–871.
6. Rowan, L.C.; Mars, J.C. Lithologic mapping in the Mountain Pass, California area using advanced spaceborne thermal emission and reflection radiometer (ASTER) data. *Remote Sens. Environ.* **2003**, *84*, 350–366.
7. Momose, A.; Miyatake, S.; Arvelyna, Y.; Nguno, A.; Mhopjeni, K.; Sibeso, M.; Muyongo, A.; Muvangua, E. Mapping pegmatite using HyMap data in southern Namibia. In Proceedings of the 2011 IEEE International Geoscience and Remote Sensing Symposium (IGARSS), Vancouver, BC, Canada, 2011; pp. 2216–2217.
8. Hernandez, E.A.; Filho, C.R. Spectral reflectance and eissivity features of PO4-bearing carbonatitic rocks from the Catalão I and Tapira complexes: New constraints for detection of igneous phosphates with remote sensing data. In Proceedings of the Anais XVI Simpósio Brasileiro de Sensoriamento Remoto-SBSR; Foz do Iguaçu, Brasil, 13–18 April 2013.
9. Bedini, E. Mapping lithology of the Sarfartoq carbonatite complex, southern West Greenland, using HyMap imaging spectrometer data. *Remote Sens. Environ.***2009**, *113*, 1208–1219.
10. Dai, J.; Wang, D.; Wang, R.; Chen, Z. Quantitative estimation of concentrations of dissolved rare earth elements using reflectance spectroscopy. *J. Appl. Remote Sens.* **2013**, *7*, doi:10.1117/1.JRS.7.073513.
11. Bedini, E.; Tukiainen, T. Using spectral mixture analysis of hyperspectral remote sensing data to map lithology of the Sarfartoq carbonatite complex, southern West Greenland. *Geol. Surv. Den. Greenl. Bull.* **2009**, *17*, 69–72
12. Van der Meer, F.D.; van der Werff, H.M.A.; van Ruitenbeek, F.J.A.; Hecker, C.A.; Bakker, W.H.; Noomen, M.F.; van der Meijde, M.; Carranza, E.J.M.; de Smeth, J.B.; Woldai, T. Multi- and hyperspectral geologic remote sensing: A review. *Int. J. Appl. Earth Obs. Geoinf.* **2012**, *14*, 112–128.

13. Cloutis, E.A. Hyperspectral geological remote sensing: Evaluation of analytical techniques. *Int. J. Remote Sens.* **1996**, *17*, 2215–2242.
14. Mielke, C.; Boesche, N.K.; Rogass, C.; Kaufmann, H.; Gauert, C.; de Wit, M. Spaceborne mine waste mineralogy monitoring in South Africa, applications for modern push-broom missions: Hyperion/OLI and EnMAP/Sentinel-2. *Remote Sens.* **2014**, *6*, 6790–6816.
15. Townsend, T.E. Discrimination of iron alteration minerals in visible and near-infrared reflectance data. *J. Geophys. Res.* **1987**, *92*, 1441–1454.
16. White, W.B. Diffuse-reflectance spectra of rare-earth oxides. *Appl. Spectrosc.* **1967**, *21*, 167–171.
17. Dieke, G.H.; Crosswhite, H.M. The spectra of the doubly and triply ionized rare earths. *Appl. Opt.* **1963**, *2*, 675–686.
18. Williams, M.L.; Jercinovic, M.J.; Harlov, D.E.; Budzyń, B.; Hetherington, C.J. Resetting monazite ages during fluid-related alteration. *Chem. Geol.* **2011**, *283*, 218–225.
19. ASD Inc Field Spec 3 HR (Build in 2010). Available online: http://www.sphereoptics.de/en/spectrometers/docs/Field%20Spec%203%20HR%202010.pdf (accessed on 1 April 2015).
20. Leonard, J.P.; Nolan, C.B.; Stomeo, F.; Gunnlaugsson, T. Photochemistry and photophysics of coordination compounds: Lanthanides. *Top. Curr. Chem.* **2007**, *281*, 1–43.
21. Kumar, G.A.; Riman, R.E.; Diaz Torres, L.A.; Banerjee, S.; Romanelli, M.D.; Emge, T.J.; Brennan, J.G. Near-infrared optical characteristics of chalcogenide-bound Nd3+ molecules and clusters. *Chem. Mater.* **2007**, *19*, 1610–1620.
22. Turner, D.J.; Rivard, B.; Groat, L.A. Visible and short-wave infrared reflectance spectroscopy of REE fluorocarbonates. *Am. Mineral.* **2014**, *99*, 1335–1346.
23. Boesche, N.K.; Rogaß, C.; Mielke, C.; Kaufmann, H. Hyperspectral digital image analysis and geochemical analysis of a rare earth elements mineralized intrusive complex (fen carbonatite complex in Telemark region, Norway). In Proceedings of 34th EARSeL Symposium; Warsaw, Poland, 16–20 June 2014.
24. Ramberg, D.I.B. Gravity studies of the Fen complex, Norway, and their petrological significance. *Contrib. Mineral. Petrol.* **1973**, *38*, 115–134.
25. Mitchell, R.H.; Brunfelt, A.O. Rare earth element geochemistry of the Fen alkaline complex, Norway. *Contrib. Mineral. Petrol.* **1975**, *52*, 247–259.
26. Andersen, T. Evolution of peralkaline calcite carbonatite magma in the Fen complex, southeast Norway. *Lithos* **1988**, *22*, 99–112.
27. Andersen, T. Magmatic fluids in the Fen carbonatite complex, S.E. Norway. *Contrib. Mineral. Petrol.* **1986**, *93*, 491–503.
28. Lie, A.; Ostergaard, C. *The Fen carbonatite complex, Ulefoss, Norway*; 21st NORTH: Svendborg, Denmark, 2011
29. Norsk Elektro Optikk. HySpex VNIR 1600/SWIR320 m-e. Available online: http://www.sphereoptics.de/de/spektrometer/docs/HySpex-GenerellMail.pdf (accessed on 1 April 2015).
30. Sunshine, J.M.; Pieters, C.M.; Pratt, S.F. Deconvolution of mineral absorption bands: An improved approach. *J. Geophys. Res.: Solid Earth* **1990**, *95*, 6955–6966.
31. Ben-Dor, E.; Chabrillat, S.; Demattê, J.A.M.; Taylor, G.R.; Hill, J.; Whiting, M.L.; Sommer, S. Using imaging spectroscopy to study soil properties. *Remote Sens. Environ.* **2009**, *113*, S38–S55.

32. Guanter, L.; Richter, R.; Moreno, J. Spectral calibration of hyperspectral imagery using atmospheric absorption features. *Appl. Opt.* **2006**, *45*, 2360–2370.
33. Harsdorf, S.; Reuter, R. Stable deconvolution of noisy lidar signals. In Proceedings of 2000 EARSeL-SIG-Workshop, Dresden, Germany, 16–17 June 2000.
34. Sunshine, J.M.; Pieters, C.M. Estimating modal abundances from the spectra of natural and laboratory pyroxene mixtures using the modified Gaussian model. *J. Geophys. Res.: Planets* **1993**, *98*, 9075–9087.
35. Zuleger, E.; Erzinger, J. Determination of the REE and Y in silicate materials with ICP-AES. *Fresenius' Z. Anal. Chem.* **1988**, *332*, 140–143.
36. Sun, S.-S.; McDonough, W.F. Chemical and isotopic systematics of oceanic basalts: Implications for mantle composition and processes. *Geol. Soc. Lond. Spec. Publ.* **1989**, *42*, 313–345.
37. Thermo Scientific Niton_XL3t_GOLDD. Available online: http://www.niton.com/docs/literature/Niton_XL3t_GOLDD_Spec_Sheet.pdf?sfvrsn=2 (accessed on 1 April 2015).
38. Jeol USA Inc. JEOL USA JXA-8230 SuperProbe Electron Probe Microanalyzer (EPMA). Available online http://www.jeolusa.com/PRODUCTS/MicroprobeandAuger/JXA-8230/tabid/223/Default.aspx (accessed on 1 April 2015).
39. Hornig-Kjarsgaard, I. Rare earth elements in sövitic carbonatites and their mineral phases. *J. Petrol.* **1998**, *39*, 2105–2121.
40. Misra, S.N.; Mehta, S.B.; Balar, B.M.; John, K. Absorption difference and comparative absorption spectrophotometry of neodymium(III) haloacetates in non-aqueous media and in Crystalline State. *Synth. React. Inorg. Met.-Org. Chem.* **2006**, *22*, 729–757.